




OPEN

Redox-based ion-gating reservoir consisting of (104) oriented LiCoO₂ film, assisted by physical masking

Kaoru Shibata^{1,2,3}, Daiki Nishioka^{1,2,3}, Wataru Namiki¹, Takashi Tsuchiya^{1,2,3} , Tohru Higuchi² & Kazuya Terabe¹

Reservoir computing (RC) is a machine learning framework suitable for processing time series data, and is a computationally inexpensive and fast learning model. A physical reservoir is a hardware implementation of RC using a physical system, which is expected to become the social infrastructure of a data society that needs to process vast amounts of information. Ion-gating reservoirs (IGR) are compact and suitable for integration with various physical reservoirs, but the prediction accuracy and operating speed of redox-IGRs using WO₃ as the channel are not sufficient due to irreversible Li⁺ trapping in the WO₃ matrix during operation. Here, in order to enhance the computation performance of redox-IGRs, we developed a redox-based IGR using a (104) oriented LiCoO₂ thin film with high electronic and ionic conductivity as a trap-free channel material. The subject IGR utilizes resistance change that is due to a redox reaction ($\text{LiCoO}_2 \rightleftharpoons \text{Li}_{1-x}\text{CoO}_2 + x\text{Li}^+ + xe^-$) with the insertion and desertion of Li⁺. The prediction error in the subject IGR was reduced by 72% and the operation speed was increased by 4 times compared to the previously reported WO₃, which changes are due to the nonlinear and reversible electrical response of LiCoO₂ and the high dimensionality enhanced by a newly developed physical masking technique. This study has demonstrated the possibility of developing high-performance IGRs by utilizing materials with stronger nonlinearity and by increasing output dimensionality.

Reservoir computing (RC) is attracting attention as a fundamental technology for the future data society, which will require high-speed, high-performance information processing of big data¹. RC is a computational framework suitable for machine learning of time-series data, and a high-speed learning model with low computational cost compared to deep learning because fewer parameters are updated during learning^{2–7}. It uses a reservoir to convert time-series input into spatiotemporal patterns, and enables pattern analysis with simple learning algorithms. Physical reservoirs are reservoir implementations that use various physical systems. Various types of physical reservoirs have been reported, such as soft bodies, optical devices, spin torque oscillators, and memristors^{4,8–27}. Nonlinearity, high dimensionality, and short-term memory are required for reservoirs to achieve high computational performance, which is the focus of the construction of physical reservoir systems^{1–7}.

In addition to computation performance, size is important for the implementation of RC devices to integrated circuits. We have recently reported ion-gating reservoirs (IGR) that are particularly small, and thus suitable for integration^{25,26}. IGR is a physical reservoir in the form of nanoionics-based transistors in which electrochemical phenomena are utilized to modulate channel resistance^{28–36}, which function is useful to perform RC^{25,26}. While there are two types of IGRs; redox-IGR and electric double layer (EDL)-IGR, the redox-IGR that uses Li_xWO₃ as a channel material showed lower computational performance and operating speed²⁶. Recent investigations on the redox reaction of WO₃ with Li⁺ have pointed out that, during cycled insertion and desertion of Li⁺ into WO₃, some of the inserted Li⁺ is irreversibly trapped in the WO₃ matrix^{37–39}. This supports the contention that the relatively low performance of WO₃ redox-IGR originates from irreversible Li⁺ trapping and that the computational performance is low due to loss of the echo state property, which is an important property of reservoirs². This indicates that redox-IGR with alternative channel materials, that do not exhibit such irreversible Li⁺ trapping, can obtain higher computing performance^{37–39}.

¹Research Center for Materials Nanoarchitectonics (MANA), National Institute for Materials Science (NIMS), 1-1 Namiki, Tsukuba, Ibaraki 305-0044, Japan. ²Department of Applied Physics, Faculty of Science, Tokyo University of Science, 6-3-1 Nijjuku, Katsushika, Tokyo 125-8585, Japan. ³These authors contributed equally: Kaoru Shibata and Daiki Nishioka. ✉email: TSUCHIYA.Takashi@nims.go.jp

To enhance redox-IGR performance, we developed a redox-IGR using a (104) oriented LiCoO₂ thin film, with high electronic and ionic conductivity, as a trap-free channel material. The subject LiCoO₂ redox-IGR utilizes the resistance change that results from the redox reaction ($\text{LiCoO}_2 \rightleftharpoons \text{Li}_{1-x}\text{CoO}_2 + x\text{Li}^+ + xe^-$) accompanying the insertion and desertion of Li⁺^{40–42}. It was determined from the results of a nonlinear autoregressive moving average (NARMA) task, a typical benchmark to evaluate RC's computational performance, that the normalized mean squared error (NMSE), which indicates the calculation error, was 0.054, which equates to 67% lower than that of WO₃ redox-IGR (NMSE = 0.163), and that the operation speed was 4 times faster²⁶. The significant improvement in computational performance was analyzed from the perspectives of the nonlinearity, high dimensionality, and short-term memory of the device. Short-term memory was measured by the device's memory capacity (MC), which was found to be lower compared to the WO₃ redox-IGR; the MC of the LiCoO₂ redox-IGR = 2.36, while the MC of the WO₃ redox-IGR = 3.57. Despite having a lower MC, the superior nonlinearity and high dimensionality of the LiCoO₂ redox-IGR led to the improvement of its computational performance²⁶. While physical reservoirs require nonlinearity, high dimensionality, and short-term memory, enhancement of nonlinearity and high dimensionality improves computing performance only in the case with sufficient short-term memory for a specific task. Gate voltage (V_G) sweep measurements of the LiCoO₂ redox-IGR showed a more nonlinear resistance change with respect to the V_G , which was attributed to the nonlinear composition change of LiCoO₂ resulting from the insertion and desertion of Li⁺^{40–42}. The high dimensionality of the device was evaluated by measuring the correlation coefficients between the nodes used in the reservoir computation. In addition to the use of Li⁺ trap-free LiCoO₂ as the channel material, a physical masking technique that was newly developed for the present study and which was implemented by drain voltage pulse trains, also significantly contributed to the enhance computation performance of the LiCoO₂ redox-IGR. It was discovered that the physical masking can noticeably improve high dimensionality without modifying the device at all, which indicates the huge potential of the technique. Furthermore, it is possible that physical masking could be used for other physical reservoirs by employing other methods (light, magnetism, mechanical stimulation, etc.) as was done in the present study. This study demonstrates the possibility of developing high-performance RC devices by utilizing materials with stronger nonlinearity and by increasing output dimensionality.

Results and discussion

LiCoO₂ redox-IGR device structure and electrical characteristics

The general model of RC is shown in Fig. 1a. Time-series data are input to the reservoir to obtain the reservoir state vector¹. The time series data input to the reservoir is transformed nonlinearly into a high-dimensional feature space as reservoir states X_i ($i = 1, 2, \dots, N$). In a full-simulation reservoir such as an echo state network, this nonlinear transformation is performed by a complex network with activation functions defined by sigmoid functions, etc., while in a physical reservoir, it is computed directly by the nonlinear dynamics inherent in the physical system^{4,8–27}. To obtain the desired output, the readout weights w_i are trained by a simple algorithm, such as linear regression, and the reservoir output $y(k)$ is obtained by a linear combination of the reservoir state $X_i(k)$ and the weights w_i as follows:

$$y(k) = \sum_{i=1}^N w_i X_i(k) + b. \quad (1)$$

Here, N , k and b are the reservoir size, discrete time step and bias, respectively.

A schematic of our LiCoO₂ redox-IGR, implemented for physical reservoir computing, and cross-sectional scanning electron microscopy (SEM) micrograph of a LiCoO₂ redox-IGR, are shown in Fig. 1b. Ti (5 nm)/Pt (35 nm) source and drain electrodes were deposited by electron beam evaporation on the surface of a SrTiO₃ (100) substrate. LiCoO₂ film (100 nm) was deposited by pulsed laser deposition (PLD) using an Nd:YAG laser operating at 266 nm wavelength, with an O₂ gas fixed flow supplied at a rate of 5.4 sccm. The substrate temperature was kept at 600 °C during deposition. Li₃PO₄ (300 nm) and Si (20 nm) were deposited by the RF sputtering method at room temperature using Li₃PO₄ and Si targets, respectively, with a supply of pure Ar gas at a fixed flow rate of 10 sccm. Sputtering times were 180 min for Li₃PO₄ target and 8 min for Si target, respectively. And sputtering power and pressure were 50 W and 0.93 Pa for both Li₃PO₄ and Si targets. We chose the amorphous Li₃PO₄ because it owns compatibility with relatively high Li⁺ conductivity and stability. That is the reason why the amorphous Li₃PO₄ is widely used as a solid electrolyte for solid-state batteries^{43,44}. Si was used for the gate electrode, since it is a promising material for the anodes of solid-state lithium batteries due to its high Li capacitance and low working electric potential^{29,40}. A Pt current collector (50 nm) was deposited on the Si by electron beam evaporation. Two drain electrodes and a source electrode were fabricated so that the channel lengths were 5 and 20 μm, with a channel width of 500 μm as shown in lower left panel of Fig. 1b.

Figure 1c shows the XRD pattern for a LiCoO₂ thin film on a SrTiO₃ single crystal. The diffraction peak observed at 2θ of 45.24° is assigned to LiCoO₂ (104)⁴⁵ (JCPDS card no. 75-0532). Fabricated LiCoO₂ thin film has no impurity phase, since there was no peak originating from other than (104). The lattice spacing calculated from the diffraction peak was 2.00 Å, which is in very good agreement with the bulk value of 2.00 Å⁴⁶. Cross-sectional TEM observation of the LiCoO₂/SrTiO₃ interface shown in Fig. 1d was performed in order to obtain more detailed information on its crystallinity. Electron diffraction of the LiCoO₂ shows that the LiCoO₂ grew in 104 orientations, perpendicular to the substrate surface, which result is the same as for the XRD pattern. Furthermore, clear diffraction spots can be seen for directions parallel to the substrate surface, indicating that the LiCoO₂ thin film has high crystallinity with aligned in-plane orientation.

By using a (104)-oriented Li⁺-hole mixed conduction LiCoO₂ thin film as a channel, which exhibits high hole and ion conductivity⁴⁶, we investigated the improvement of device operating speed and computational performance through the rapid and smooth insertion and desertion of Li⁺. By application of a V_G , this IGR

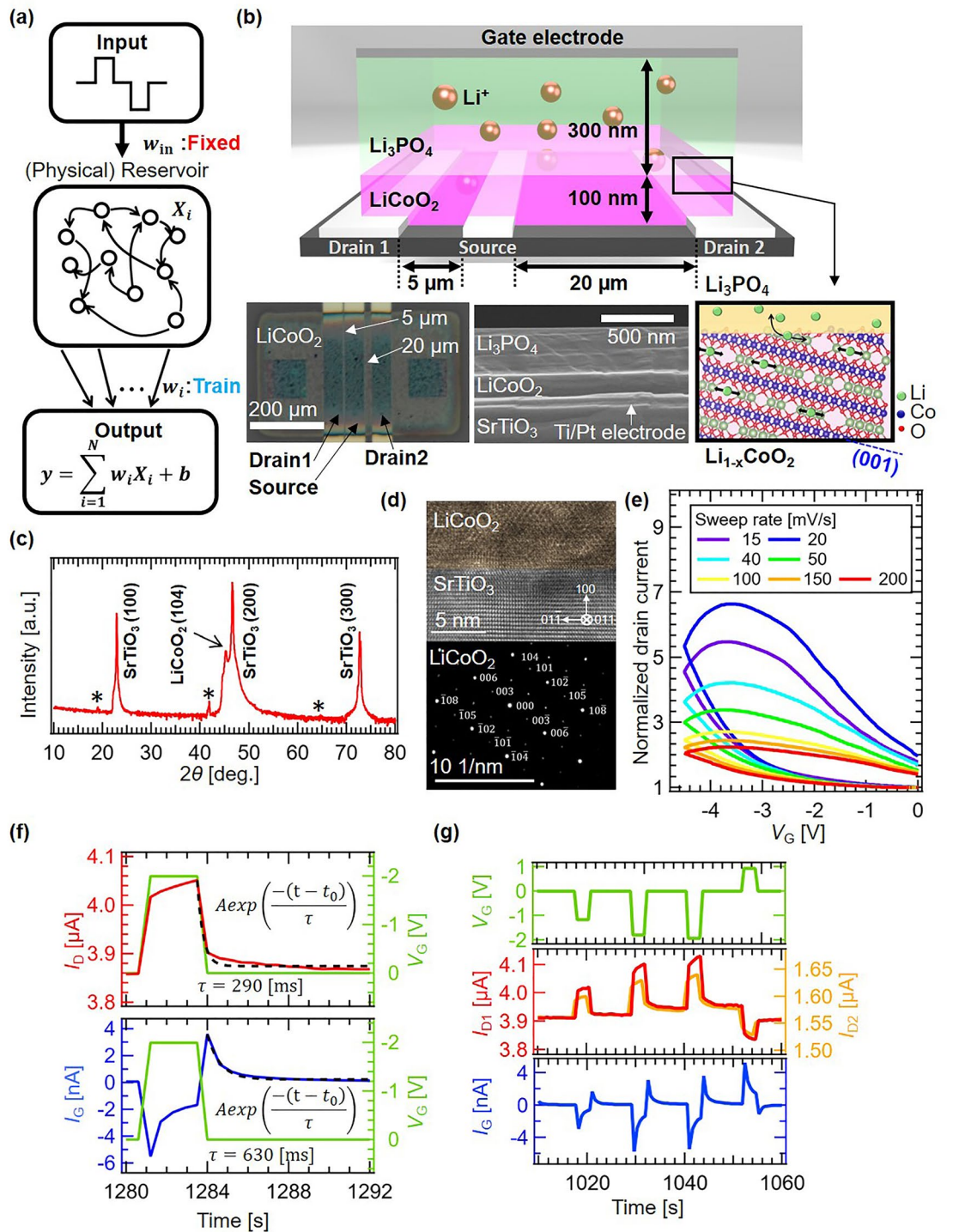
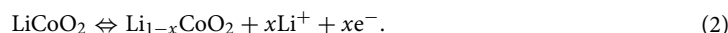


Figure 1. (a) General scheme of the subject reservoir computing system with (Physical) reservoir. w_{in} and w_i denote the input weight and read-out weight, respectively. (b) Schematic image of LiCoO₂-based redox-ion-gating reservoir, cross-sectional SEM micrograph of a LiCoO₂ redox-IGR, and insertion (desertion) of Li⁺ in (104) oriented LiCoO₂. (c) XRD pattern of LiCoO₂/SrTiO₃. Stars mark the $k\beta$ diffraction peaks. (d) Cross-sectional TEM image and electron diffraction of LiCoO₂/SrTiO₃. (e) Normalized I_D-V_G curve of the subject redox-IGR during V_G sweeping from 0 to -4.5 V. (f) Changes in drain (Upper) and gate (Lower) currents when a single pulse of V_G is applied. (g) (Upper) V_G pulse stream input, (Middle) I_{D1} and I_{D2} response, and (Lower) I_G response during operation of the redox-ion-gating reservoir.

changes the channel resistance by inserting (deserting) Li⁺ into (from) the channel through the redox reaction shown below as Eq. (2):



When a negative V_G is applied, Li^+ are removed from the channel (i.e., x increases) and move through the solid electrolyte to the Si gate electrode shown in the lower panel of Fig. 1b. During the removal of Li^+ from the channel, Co^{3+} is oxidized to Co^{4+} and electron holes are generated to maintain charge neutrality. This is accompanied by an increasing in the electrical conductivity of the $\text{Li}_{1-x}\text{CoO}_2$. This reaction in high quality LiCoO_2 thin film is highly reversible^{40–42,46}, so when a positive V_G is applied, the conductivity of the channel decreases as Li^+ are inserted into the channel (i.e., x decreases). To measure the resistance modulation of the channel with respect to the V_G , we measured the drain current (I_D) during V_G sweeping.

The electrical characteristics of the fabricated device were analyzed at room temperature, in a vacuum chamber, using the source measurement unit (SMU) of a semiconductor parameter analyzer (4200A-SCS, Keithley). Materials in our devices were so stable that we could fabricate our devices in air, although we performed electrical measurements in vacuum for keeping our devices in the best condition. Such condition can be easily obtained by using encapsulation technology⁴⁷, which has been well established for fabrication of integrated circuits (ICs) in commercial electronic devices. For example, transfer molding and compression molding using various types of resin (semiconductor encapsulant) are widely used to keep ICs in vacuum to protect them. Therefore, there is no severe limitation to practical applications. The normalized I_D - V_G curve of the redox-IGR is shown in Fig. 1e. The V_G was swept from 0 to -4.5 V and then back to 0 V at various sweep rates, ranging from 15 (slow) to 200 mV/s (fast). Nonlinearity in I_D change was confirmed from the I_D by the redox reactions shown in Eq. (2). These are associated with the insertion and desertion of Li^+ that changes the channel resistance, and a clear hysteresis curve can be drawn at any sweep rate, which suggests that the device exhibits short-term memory, which in turn is a necessary function for reservoirs^{1–7}. Generally, a dynamical system with a specific time constant shows a hysteresis when an external stimulation with a time constant, which is close to the one of the dynamical systems, is applied. In contrast, when the input is sufficiently faster than the time constant of the dynamical system, the response does not follow and does not show hysteresis. Also, when the input is sufficiently slow, the response corresponds to the steady state of the system and does not show hysteresis. Therefore, the extent of hysteretic behavior has a peak with respect to the speed of external stimulation. In the present case shown in Fig. 1e, the hysteresis of 20 mV/s is larger than the one of 15 mV/s because the sweep rate of 20 mV/s is closer to the peak discussed above.

Changes in drain and gate currents when a single pulse of gate voltage is applied are shown in the Fig. 1f. Each current relaxation was fitted with Eq. (3) as shown in black dotted lines.

$$f(t) = y_0 + A \exp\left(\frac{-(t-t_0)}{\tau}\right) \quad (3)$$

Relaxation time τ was 290 and 630 ms, respectively. (The other fitting parameters and details of the fitting can be found in Supplementary Table S1). The drain and gate currents show a relaxation with respect to the pulse input, indicating that the device has short-term memory. Different drain and gate current relaxation times enhance the diversity of the nodes and improve computational performance. In particular, the gate current has a nonlinear and complex response to the V_G pulse, and the complex response is expected to lead to higher computational performance as in EDL-IGRs²⁵. Our IGR utilized such nonlinear I_D , I_G responses to Li^+ insertion and desertion into LiCoO_2 channel, driven by V_G input, as the nonlinear dynamics function that makes it possible for physical reservoirs to perform information processing.

The subject IGR is operated by a V_G pulse stream^{25,26}. The time-course nonlinear response of I_D and the gate current (I_G) outputs are shown in Fig. 1g. The upper panel of the figure shows the V_G pulse stream, which is the input from the IGR. The middle panel of the figure shows that different responses were obtained by using the two drain electrodes with different channel lengths. Upon application of the V_G pulse stream, the effective potential drops on the two channels are different due to different channel resistance, which is useful to enhance the diversity of the I_D response²⁵. Since the I_G has a different shape and nonlinearity from I_D , the I_G shown in the lower panel of the figure was also used in the reservoir calculation²⁶. The behavior of the I_G is different from the I_D , and the use of the I_G in the calculation is expected to enhance the high dimensionality of the reservoir and to significantly improve its computational performance.

Concerning the relatively slow operation speed, it can contribute to process a time-series data with slow change. In order to process time series data with a specific speed, response speed of the physical reservoir should cover the dynamics of the data. Therefore, in order to process a time-series data with slow change, the physical reservoir with slow response to input signal is needed. A typical example of that is the predication task of blood glucose level with slow change, which exhibits several ups and downs over several hours in a day⁴⁸.

Physical masking, for high dimensionality enhancement, implemented by drain voltage pulses

Masking is a pre-processing of input whereby the dimensionality of a physical reservoir system is effectively maximized^{1,49}. In order to achieve high dimensionality, which is one of the characteristics required for reservoirs, the number of outputs (reservoir states) obtained from the reservoir for a given input must greatly exceed the input dimension. In system reservoirs, high dimensionality can be easily achieved by increasing the network size (number of nodes), but it is generally difficult to obtain a sufficient number of reservoir states physically in a physical reservoir due to limitations such as measurement probes²⁶. Therefore, the virtual node method, which virtually considers the time evolution of the response to the input obtained from the physical system as spatially distinct nodes, is widely adopted in physical reservoirs. However, it is difficult to achieve sufficiently high dimensionality by simply using the transient responses of the physical system as different nodes in RC, because neighboring virtual nodes behave in a similar manner, and the effective number of nodes does not increase.

Thus, by combining the input signal with a masked waveform containing fluctuations (masking), the virtual nodes behave differently from each other and high dimensionality can be improved. Masking is performed by introducing a $(N_M \times Q)$ mask matrix \mathbf{M} for the Q -dimensional input signal $\mathbf{u}(k)$, as follows:

$$\mathbf{J}(k) = \mathbf{M} \times \mathbf{u}(k). \quad (4)$$

Here, N_M and $\mathbf{J}(k)$ are the number of mask dimensions and the masked input signal, respectively; \mathbf{M} is always fixed at times k , and a random number sequence or random bit sequence is used. For example, the masked input $\mathbf{J}(k)$ is an N_M -dimensional vector if $Q = 1$. When $\mathbf{J}(k)$ is actually input to the physical system, these N_M elements are input to the physical system at a fixed time interval θ . Then, after completing input of the N_M masked input signals (i.e., after $\theta \times N_M$ has elapsed in real time t), the next step of input $\mathbf{J}(k + 1)$ is performed in the same manner. In this way, masked input is generated by synthesizing raw input with a specific mask waveform, including random ones, as a pre-processing of the input signal. By designing the mask matrix appropriately, and inputting $\mathbf{J}(k)$ at time intervals that consider the time constant of the physical system (preferably shorter than the time constant of the physical system), interaction between neighboring virtual nodes is strengthened and the high dimensionality and nonlinearity are improved^{21,49}. The left-hand and middle panels of Fig. 2a show RC without masking (left) and with masking (middle). When masking is used, time-multiplexing of the input is achieved and high dimensionality is enhanced. While masking generally leads to better computing performance, it creates an extra pre-processing calculation burden.

In the present study, a physical masking was developed and applied to the subject IGR to achieve high performance, as shown in the right-hand panel of Fig. 2a. By utilizing a structural feature of the IGR, multi-input terminals (i.e., gates and drains), a mask waveform can be directly input to the reservoir through the drain electrodes as drain voltage pulse trains, as shown in Fig. 2b. In this case, masking does not require pre-processing of the input and the masking is physically performed. Such is the physical masking we propose in this study. By utilizing a physical mask, the I_D response is changed from the one shown in the left-hand panel of Fig. 2b to the one shown in right-hand panel of Fig. 2b. Although the I_D response with physical mask seems to appear as a monotonous triangle wave, it does in fact generate reservoir states with excellent diversity. The reservoir states obtained from I_D responses (without and with physical masking) shown in Fig. 2b are compared to those in Fig. 2c. Without physical masking, reservoir states are concentrated in a narrow region from 1.92 to 2.17. Conversely, when physical masking is used, reservoir states are spread to six lines, each of which consists of diverse reservoir states. As indicated in the resulting clear differences in the versatility of reservoir states, physical masking significantly contributes to the enhancement of the computing performance of LiCoO₂ redox-IGR, as well as to the inherent Li⁺ trap-free characteristic of LiCoO₂, as shown in the following section.

Solving a second-order nonlinear dynamic equation

In order to evaluate the effect of the subject physical masking on computational performance, we solved a second-order nonlinear dynamics equation task by a redox-IGR with V_D induced physical masking, as shown in Fig. 3a^{12,15}. The target waveform $y_t(k)$ is generated by the second-order nonlinear dynamic equation shown in Eq. (5), which includes second-order nonlinearities and past data:

$$y_t(k) = 0.4y_t(k-1) + 0.4y_t(k-1)y_t(k-2) + 0.6u^3(k) + 0.1. \quad (5)$$

Here, $u(k)$ is a random input ranging from 0 to 0.5. The random input $u(k)$ was converted to a voltage pulse streams with V_G of $V_G(k)$, a pulse period T of 10 s, duty rate D of 25%, and input to the gate of the IGR. $V_G(k)$ was linearly transformed from $u(k)$ to a range of -1 V to 2 V, as follows, with $V_G = 0$ V at the pulse interval as shown in the upper panel of Fig. 2b:

$$V_G(k) = 2V_{ap}u(k) + V_{offset}. \quad (6)$$

Here, V_{ap} ($= 3$ V) and V_{offset} ($= -1$ V) are the amplitude and offset voltages, respectively. In addition to the drain currents obtained from two channels with different lengths, to achieve higher-dimensional reservoir states via the optimized physical structure, the gate currents with spikes were also used in the reservoir computing, as shown in the lower panel of Fig. 1f. This lead to enhanced high dimensionality due to the variety of reservoir states included^{25,26}. These drain currents, corresponding to the reservoir state, were measured with the following two types of drain voltages: (1) V_D without physical masking: a constant V_D of 0.4 V and (2) V_D with physical masking: a stepped triangular wave V_D with a voltage range of -0.4 V to 0.4 V, a period of $T/4$ for V_{D1} and -0.8 V to 0.8 V, and a period of $T/2$ for V_{D2} . The I_D response with and without physical masking is shown in the lower panel of Fig. 2b. While the I_D response exhibits a single relaxation-like behavior without physical masking, with physical masking, it appears as a stepped triangular wave similar to the applied V_D stream for physical masking. As will be clarified later, the output with such a triangular wave form includes sufficient variety. To further increase the higher dimensionality of the reservoir states, 20 current values per V_G pulse were obtained at virtual nodes, as shown in Fig. 2b. 20 reservoir states were obtained from each of the three current responses, so the reservoir size N of the redox-IGR was 60. The reservoir states $X_i(k)$ ($i = 1, 2, \dots, 20$) corresponding to I_{D1} are shown in Fig. 2c. When physical masking is not utilized (i.e., I_D responses were measured under constant V_D), the behavior of these reservoir states is similar and low in diversity. On the other hand, when masking (i.e., I_D responses were measured with triangular wave V_D inputs) is used, the reservoir states are clearly diverse and achieve good high dimensionality. Such high-dimensionality will be discussed later.

The reservoir output is obtained by a linear combination of the readout weights w_i which was trained by ridge regression²⁵ and the reservoir state $X_i(k)$. The computational performance of the redox-IGR in this task was evaluated by 'prediction error', as follows:

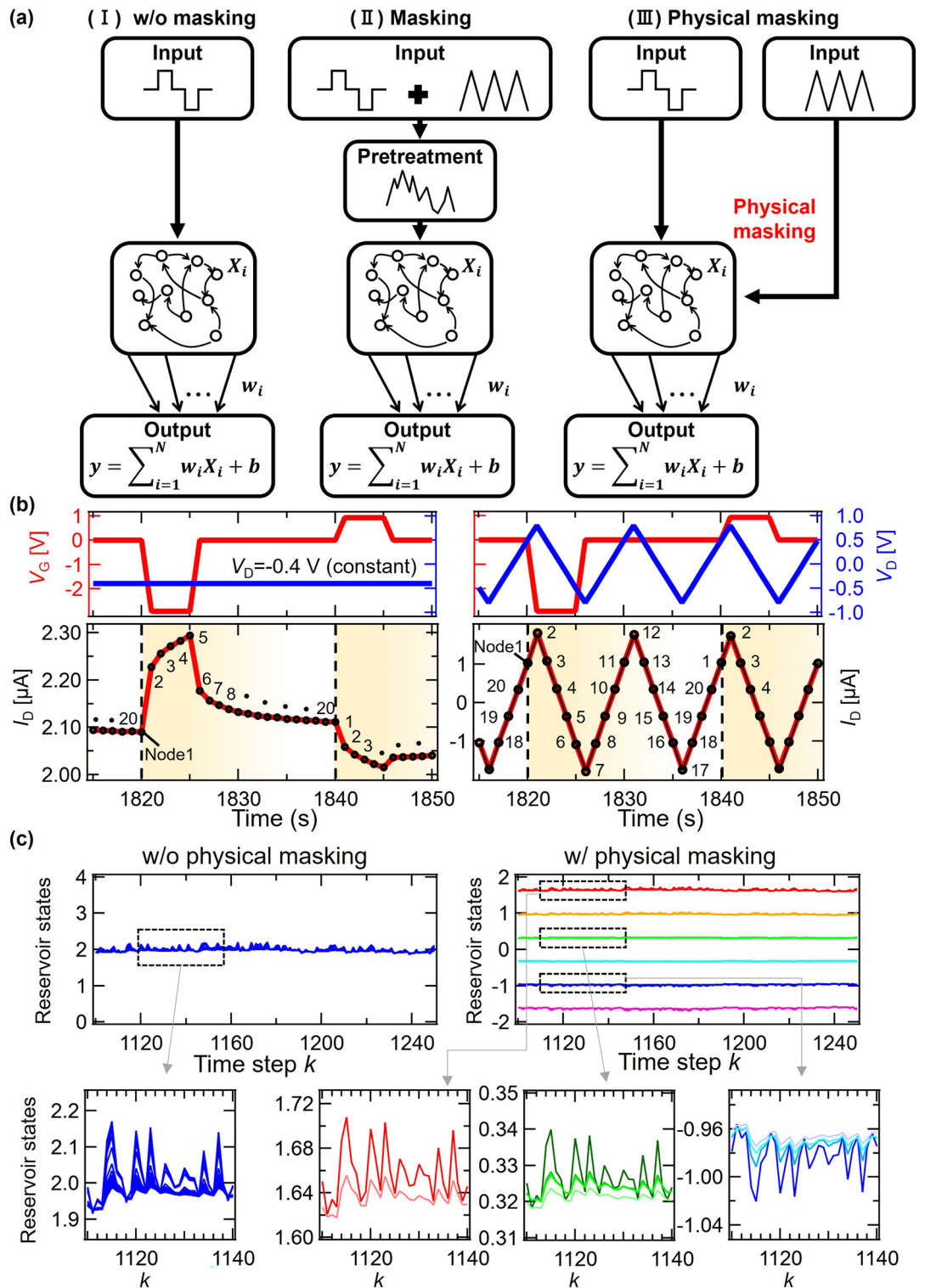


Figure 2. (a) (I) RC without masking, (II) RC with masking, and (III) RC with physical masking. (b) V_G and V_D input and I_D output w/o and w/ physical masking. (c) Reservoir state waveforms (X_1, X_2, \dots, X_{20}) w/o and w/ physical masking.

$$prediction\ error = \frac{\sum_{k=1}^n [y_t(k) - y(k)]^2}{\sum_{k=1}^n [y_t(k)]^2} \quad (7)$$

Here, n is the data length, $n = 1100$ for the training phase and $n = 150$ for the test phase. The initial 200 steps were excluded from the computation in order to wash out the initial state of the device. Figure 3b shows the predicted and target waveforms obtained without (upper panel) and with (lower panel) physical masks. The

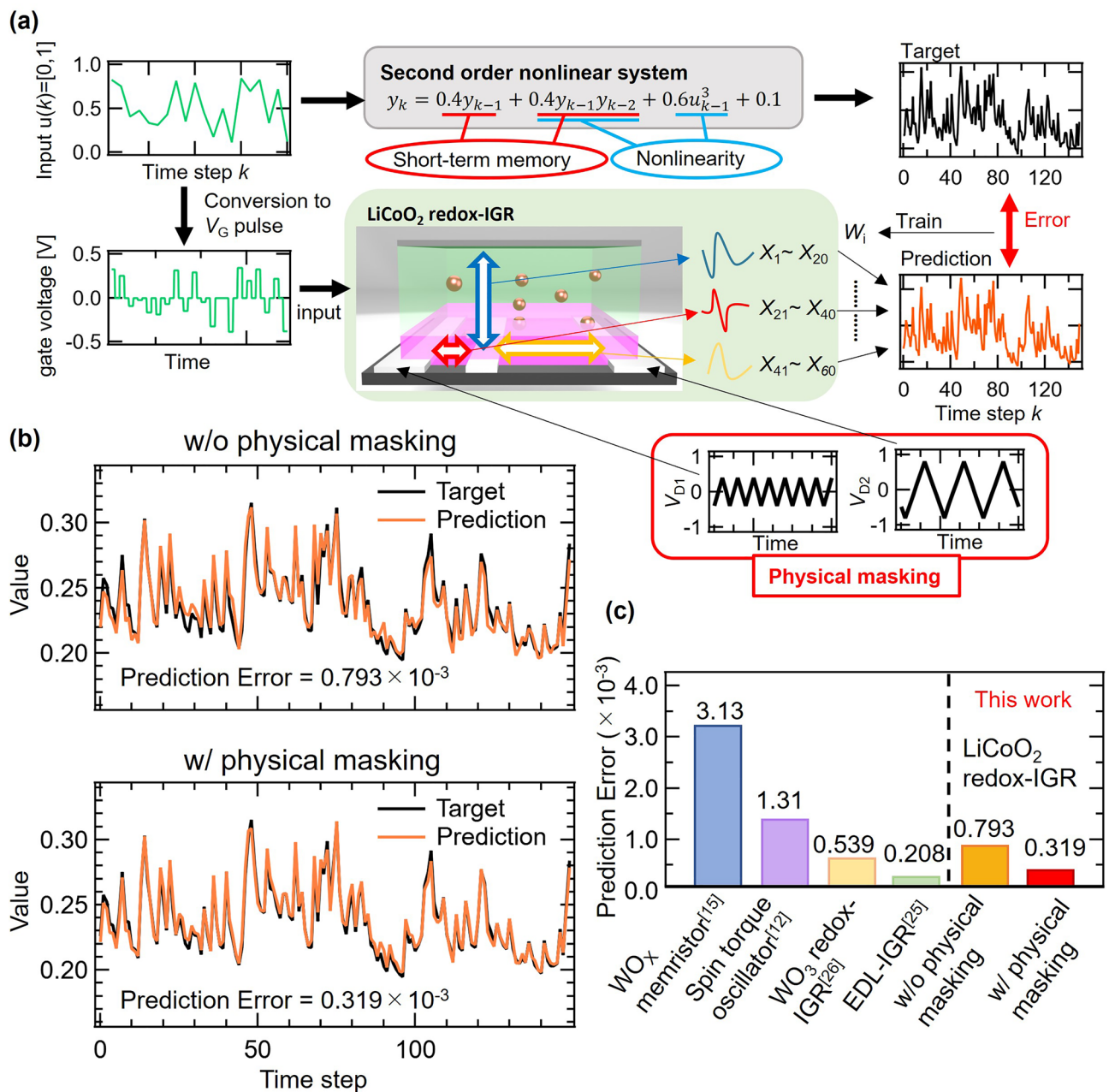


Figure 3. (a) Solving a second-order nonlinear dynamic equation task. (b) Target and prediction waveform of second-order nonlinear dynamics equation task w/o and w/ physical masking. (c) Performance comparison with other physical reservoirs.

predicted waveform and the target waveform are in better agreement with each other with masking than without physical masking, and Eq. (5) is solved more correctly when physical masking is employed. Physical masking also reduced the training error by 65% (prediction error of 6.22×10^{-4} to 2.16×10^{-4}) and the test error by 60% (prediction error of 7.93×10^{-4} to 3.19×10^{-4}). This indicates that V_D -induced physical masking is effective in improving the computational performance of redox-IGR. Also, to examine the effects of Physical masking, we performed additional experiments when two signal streams are applied to one gate electrode, and the same single stream is applied to the gate and drain electrodes. We solved a second-order nonlinear dynamics equation task. Applying two signal streams input to a single electrode is a general masking which is the pretreatment of input as shown in Fig. 2a(II) and the prediction error under the condition was 5.38×10^{-4} which was better than the case without physical masking [prediction error: 7.93×10^{-4} as shown in Fig. 3b], but worse than the case with physical masking [prediction error: 3.19×10^{-4} as shown in Fig. 3b]. When the same inputs were applied to the gate and drain electrodes, the prediction error was 1.01×10^{-3} , which was worse than the case without physical masking. Details are explained in the Supplementary Information. According to the results, the physical masking shown as (III) in Fig. 3a was the best among them.

Figure 3c shows a comparison of performance with the physical reservoirs that have been reported to date^{12,15,25,26}. Without physical masking, the computation performance was slightly lower than with WO₃ redox-IGR, but with physical masking, the computation performance greatly exceeded WO₃ redox-IGR, and the operating speed is also four times faster than that of WO₃ redox-IGR²⁶. By masking, the computational performance of the redox-IGR is further improved, making it comparable to that of EDL-IGR, which device exhibits high computational performance²⁵. This result proves that masking overcomes the challenges of conventional redox-IGRs in terms of computational performance. The reasons for the significant improvement in computational performance compared with WO₃ redox-IGR will be discussed in later sections.

Solving a NARMA2 task

In addition to the second-order nonlinear dynamic equation, a 2nd-order Nonlinear Auto Regressive Moving Average (NARMA) task was performed, being a task that requires higher computational performance^{1,25,26}; the NARMA2 task is a time series data analysis task, as shown in Eq. (8), and is a benchmark commonly used to evaluate the computational performance of RC^{24–26,50–52}.

$$y_t(k+1) = 0.4y_t(k) + 0.4y_t(k)y_t(k-1) + 0.6u^3(k) + 0.1. \quad (8)$$

The computational performance of the redox-IGR in this task was evaluated by normalized mean squared error (NMSE) as follows:

$$NMSE = \frac{1}{n} \frac{\sum_{k=1}^n [y_t(k) - \hat{y}_t(k)]^2}{\sigma^2[y_t(k)]}. \quad (9)$$

Here, n is the data length, $n = 1100$ for the training phase and $n = 150$ for the test phase.

Figure 4a shows the relationship between the NARMA2 score, pulse period T , and duty rate D . The error decreases as D decreases, and is smallest at $T = 10$ s for all D , with the smallest error NMSE = 0.118 for the condition indicated by the star in the figure ($T = 10$ s, $D = 25\%$). The target and the predicted output by IGR (test phase) under these conditions are shown in Fig. 4b. If T is too short, the resistance modulation of the LiCoO₂ channel becomes small because the insertion and desertion of Li⁺ (redox) in the channel cannot follow the fast V_G pulse change. We considered that this causes the output of the device to become too similar because there is insufficient conduction modulation, which causes a decrease in computational performance. Also, if the T is too long, the next pulse does not input even after complete relaxation of the previous input, resulting in more similar output data, which causes the low performance observed. The neighboring virtual node diversity during the relaxation was particularly reduced. Additionally, it was observed from the color map that calculation performance improves as the duty rate decreases. In contrast, EDL-IGRs show improved calculation performance with increasing duty rate, and an IGR with a duty rate of 75% exhibited the highest performance, which led to results that were different from the previous IGR²⁵. The large decrease in score (high NMSE) shown in Fig. 4a, with a duty rate of 100%, is due to the input pulse not reaching 0 V and the relaxation behavior is therefore not included in the output.

Furthermore, in order to improve computational performance within a limited number of nodes, we focused on the correlation between nodes. We reduced the calculation errors by decreasing the correlation between nodes to increase the number of nodes that are effective for computation. To reduce the correlation between the nodes, we changed the drain voltage to from a constant voltage to a triangular wave. A +0.4 to −0.4 V triangular wave at a pulse period 4 s was applied to drain electrode 1, which has a short channel length, and a +0.8 to −0.8 V triangular wave at a pulse period 10 s was applied to drain electrode 2, which has a longer channel length. As shown in Fig. 4c, the physical masking reduced the error by 72% (NMSE = 0.054) compared to when physical masking was not used. The performance of LiCoO₂ device without physical masking is inferior to the WO₃ device for second-order nonlinear dynamic equation task. In contrast, for NARMA2 task, which is much more difficult than the second-order nonlinear dynamic equation task in general, the performance of LiCoO₂ is far better than the WO₃ device regardless of with or without physical masking. Although the relatively low performance of the LiCoO₂ device was observed for the second-order nonlinear dynamic equation task and we could not clarify the reason, we believe that the performance for the NARMA2 task is more reliable index to discuss the reservoir property. By applying physical masking, redox-IGR achieve computational performance comparable to EDL-IGR, while the physical masking does not require pre-processing to achieve significant improvements in calculation performance. This technique is a highly effective method for improving calculation performance, and can also be applied to other physical reservoirs.

Figure 4d shows the relationship between NARMA2 score and reservoir volume^{24–26,50–52}. Because this device has three terminals, it is less integrated than two terminal physical reservoirs such as memristors^{12,15–19,21,22,28}. However, all the devices are composed of thin films, it is relatively smaller and more integrated than most physical reservoirs reported so far, as shown in Fig. 4d.

Relationship between the computational performance and memory capacity

We have examined the significant improvement in computational performance from the three perspectives required for reservoirs: short-term memory, nonlinearity, and high-dimensionality¹. When performing time series data analysis tasks that are dependent on past input, it is necessary for a reservoir to have short-term memory. Short-term memory was evaluated by measuring the memory capacity (MC) of the device through a short-term memory task¹. Said task examines how well the model can reconstruct past input data as current output. The degree of matching between the target waveform of delay length τ and the output waveform of the trained model can be measured by the coefficient of determination $r^2(\tau)$ shown in Eq. (10) below:

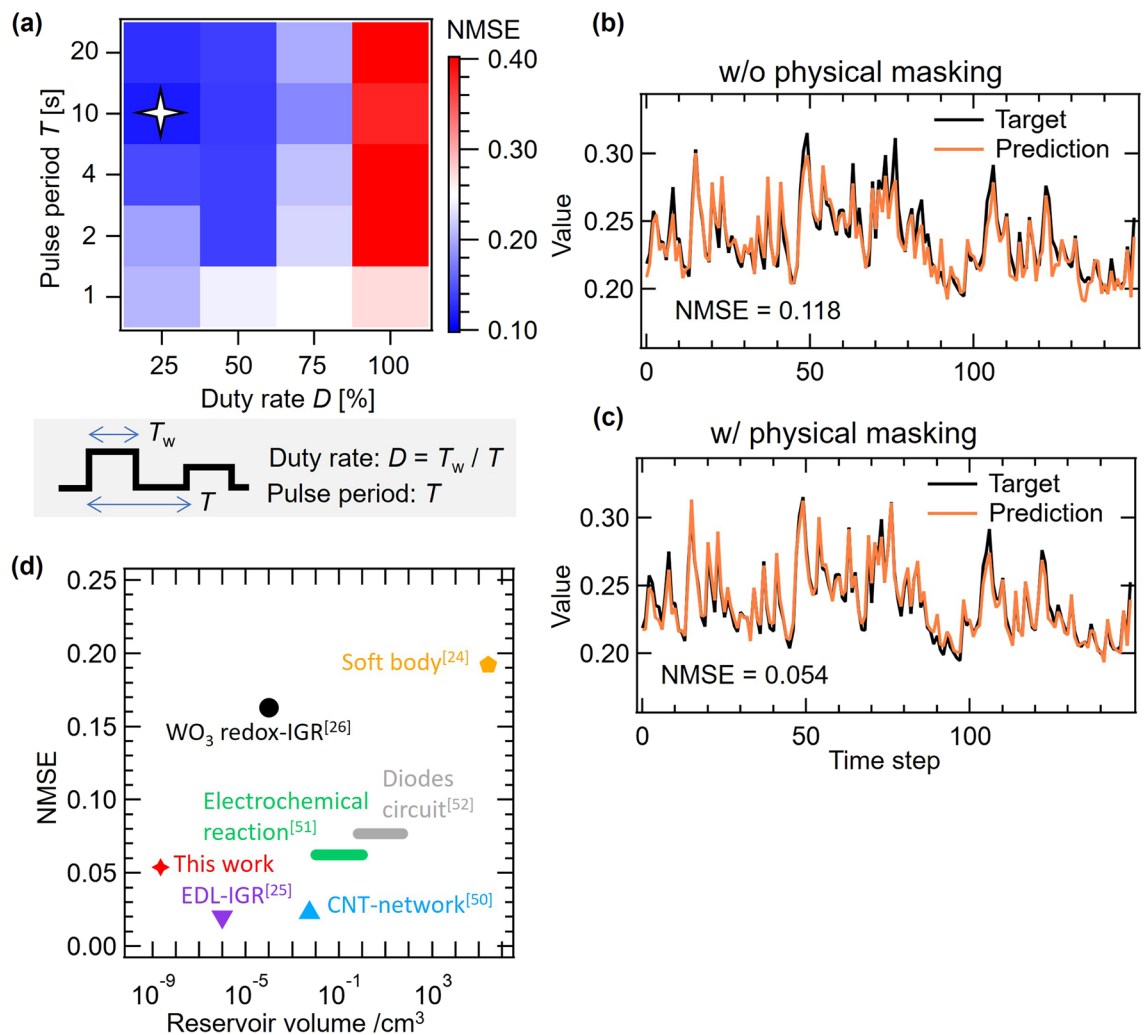


Figure 4. (a) (Upper) Relationship between NARMA2 score, pulse period T , and duty ratio D in the test phase. (Lower) Diagram of Pulse period and Duty rate D . (b,c) Target and prediction waveforms of the NARMA2 task w/o and w/ physical masking, respectively. (d) NMSEs of the NARMA2 task and reservoir volumes of various physical reservoirs. The reservoir volume of this work was calculated as the total of channel, electrolyte, and electrodes.

$$r^2(\tau) = \frac{\text{Cov}^2(u(k-\tau), \hat{y}_\tau(k))}{\text{Var}(u(k))\text{Var}(\hat{y}_\tau(k))}. \quad (10)$$

Here, $\hat{y}_\tau(k)$ represents the model output at delay length τ , $\text{Cov}(\cdot, \cdot)$ denotes covariance, and $\text{Var}(\cdot)$ represents variance, respectively. The possible range of $r^2(\tau)$ is $0 \leq r^2(\tau) \leq 1$, and if the model can successfully reconstruct the delayed sequence as the model output, $r^2(\tau)$ takes a value close to 1. The variation of $r^2(\tau)$ in respect to delay length τ is called the forgetting curve. Forgetting curves with and without physical masking are shown in Fig. 5a. MC is defined as the area under the forgetting curve, which is described as follows:

$$MC = \sum_{\tau=1}^{\infty} r^2(\tau). \quad (11)$$

In regions with a long delay length τ , there was almost no change in $r^2(\tau)$, but when compared to regions with a short delay length ($\tau \leq 2$), $r^2(\tau)$ increased when a physical mask was applied, leading to an increase in MC. Masking is known to improve interactions between virtual nodes, and is accompanied by increasing reservoir size⁴⁹. Because the upper limit of MC is determined by reservoir size, the physical masking in the study increases MC, and this increase in MC led to an increase in the computational performance of the device.

Figure 5b shows the relationship between the computation performance and MC. The downward-sloping relationships between NMSE and MC for both LiCoO_2 and WO_3 redox-IGR, approximated by the two straight lines, evidences that increased MC leads to reduced NMSE, which means improvement in the computational performance of a reservoir²⁶. It is also shown that MC increases with the application of physical masking under all experimental conditions, and the NMSE of NARMA2 is greatly reduced in LiCoO_2 redox-IGR. Although LiCoO_2 redox-IGRs are inferior to WO_3 redox-IGRs in terms of MC, the NMSE is smaller. This deviation from

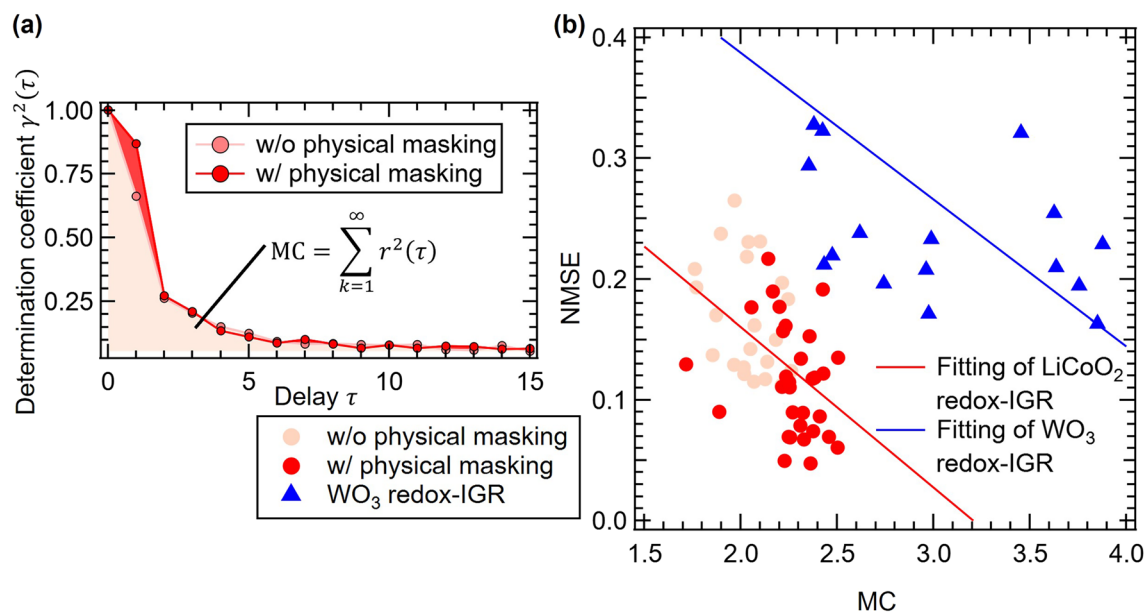


Figure 5. (a) Forgetting curves w/o and w/ physical masking. (b) Relationship between computational performance and MC.

said tendency indicates that the high computational performance achieved in this study is attributed not only to MC, but also from to other requirements (nonlinearity and/or high dimensionality)¹.

Relationship between computational performance and nonlinearity

Nonlinearity is an element required by a reservoir to enable it to transform non-linear time-series input data, which is not linearly separable into a linearly separable state. Further, strong nonlinearity improves computational performance by diversifying the output and increasing the expressive power of the model¹. We performed V_G sweep measurements in order to investigate the nonlinearity, on-off ratio, and reversibility. Figure 6a compares the normalized I_D -normalized V_G curves of a LiCoO₂ redox-IGR and a WO₃ redox-IGR²⁶. The on-off ratio of I_D is larger for the LiCoO₂ redox-IGR than for the WO₃ redox-IGR, which indicates a higher response to V_G . Focusing on the normalized I_D value at the end of the hysteresis curve, LiCoO₂ redox-IGRs are closer to the initial current value than WO₃ redox-IGRs, which means that LiCoO₂ has better charge-discharge reversibility than WO₃, and the device behavior is less likely to change even if a pulse voltage is repeatedly applied during calculation. This is quite reasonable if one considers an irreversible Li⁺ trapping into a WO₃ matrix during redox cycles, as has been reported recently^{37–39}. It further means that the LiCoO₂ redox-IGR has high reproducibility as a time-series input-output converter, and the same time-series output can be obtained for the same time-series input, without depending on random initial conditions. Such good reproducibility in the LiCoO₂ redox-IGR leads to the achievement of the echo state property, which is an important property required for reservoirs, regardless of whether they are simulated or physical reservoirs².

To evaluate nonlinearity, we compared the correlation coefficients of the I_D - V_G curve and the linear line ($I_D = -V_G$). The correlation coefficient, calculated by Eq. (12), is a measure of how linear the I_D - V_G curve is; if the linearity is high, the correlation coefficient is close to 1, and if the linearity is low, the correlation coefficient is close to 0.

$$R(x_i, y_i) = \frac{\sum_{i=1}^n (x_i - \bar{x})(y_i - \bar{y})}{\sqrt{\sum_{i=1}^n (x_i - \bar{x})^2} \sqrt{\sum_{i=1}^n (y_i - \bar{y})^2}}. \quad (12)$$

In Eq. (12), n represents the total number of data points, x_i and y_i are the value of normalized drain current and the value of the linear function, respectively. \bar{x} , \bar{y} are the average of each value. Regarding the correlation coefficient with a linear line and an I_D - V_G curve, the correlation coefficients for the LiCoO₂ redox-IGR and WO₃ redox-IGR are 0.882 and 0.964, respectively, which shows that the LiCoO₂ redox-IGR has a more nonlinear change than the WO₃ redox-IGR (Fig. 6b). Nonlinearity is one of the main functions required of reservoirs in nonlinear transformations of time series input data, and it is known that the higher nonlinearity of systems can increase their computational performance¹. We attribute the observed performance improvement to the strong nonlinearity of the resistance modulation in the LiCoO₂ redox-IGR, evidenced by the I_D - V_G curve.

In order to consider the origin of the nonlinearity, we further analyzed the electrical characteristic of the LiCoO₂ redox-IGR. Figure 6c shows variation in x in Li_{1-x}CoO₂ and hole mobility with respect to V_G , which are derived from the I_D - V_G and I_G - V_G curves. x showed nonlinear variation in the range from 0.02 to 0.08, which is relatively close to that found in stoichiometric LiCoO₂. On the other hand, hole mobility is also nonlinearly changed, from 1.8×10^{-3} to 5.0×10^{-4} . Near the stoichiometric region, the mechanism of hole transport in LiCoO₂

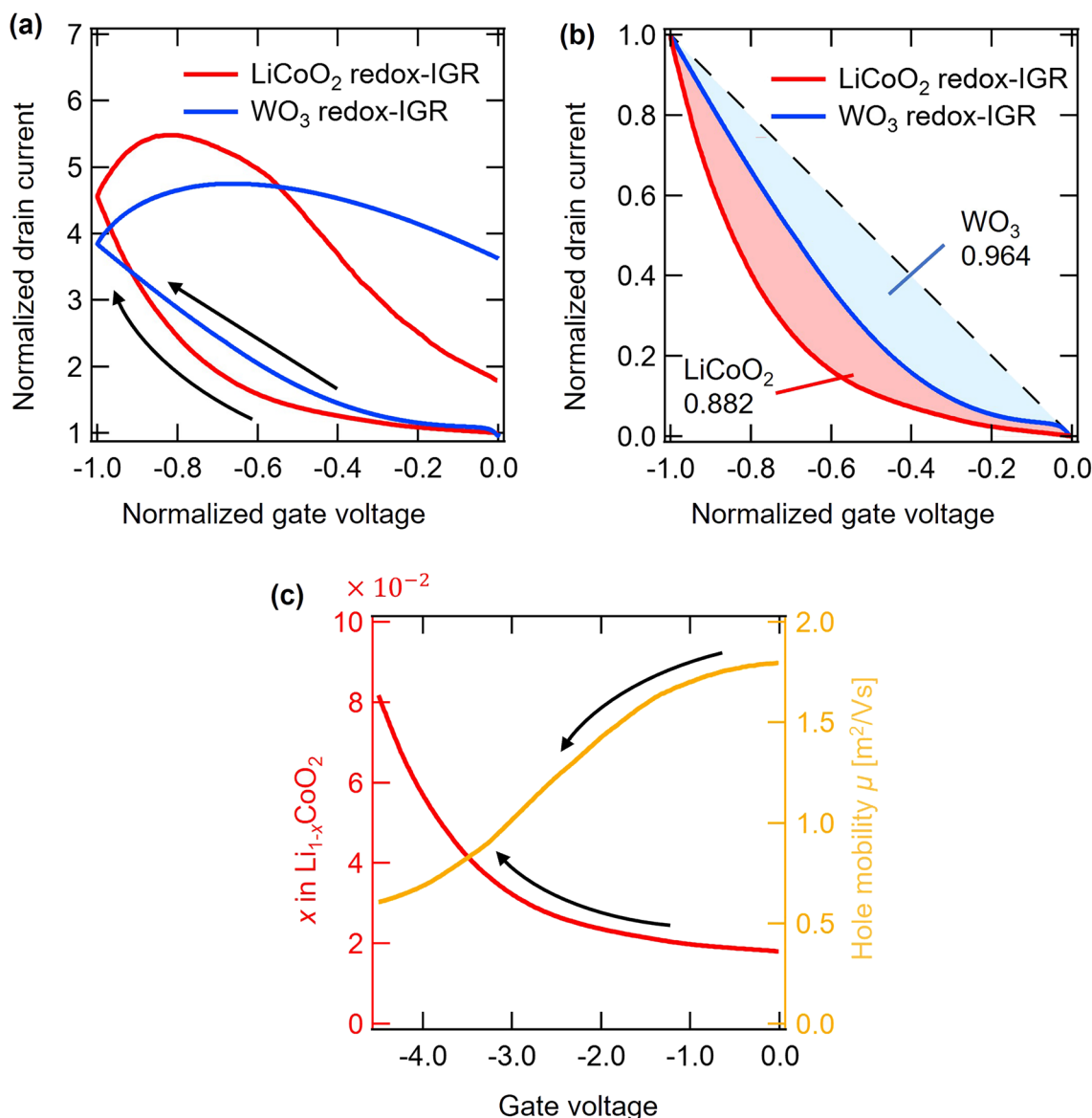


Figure 6. (a) Comparison of normalized I_D – normalized V_G curve of the LiCoO₂ redox-IGR and WO₃ redox-IGR. (b) Comparison of Nonlinearity in I_D – V_G curve. (c) x in Li_{1-x}CoO₂ and hole mobility change of LiCoO₂ in V_G sweep.

was reported to be variable-range hopping, which is characteristic of Anderson type insulator–metal transition, and the mobility observed in the present study is consistent with such report^{53,54}. The origin of the strong nonlinearity of the LiCoO₂ redox-IGR is attributed to nonlinear changes of both x and hole mobility.

Relationship between computational performance and high dimensionality

In addition to MC and nonlinearity, another important condition required for reservoirs is high dimensionality¹. High dimensionality facilitates pattern recognition in the readout section by mapping time-series input data to a high-dimensional space. For physical reservoirs, it is important how the number of effective nodes is increased while maintaining low correlation among a limited number of nodes. High dimensionality can be evaluated by the number of effective nodes used in the calculation, which in this case was evaluated by the correlation coefficient $r(X_i, X_j)$ between each node, using the following equation,

$$r(X_i, X_j) = \frac{\sum_{k=1}^{L=150} (X_i(k) - \bar{X}_i)(X_j(k) - \bar{X}_j)}{\sqrt{\sum_{k=1}^{L=150} (X_i(k) - \bar{X}_i)^2} \sqrt{\sum_{k=1}^{L=150} (X_j(k) - \bar{X}_j)^2}}. \quad (13)$$

Here, X_i and L are the reservoir state of node i and the data length, respectively. The correlation coefficient is a measure of how similar each node is; if the similarity is high, the correlation coefficient is close to 1, and if the similarity is low, the correlation coefficient is close to 0. Figure 7a shows the reservoir state wave form for node 7 (X_7 , red line) and node 40 (X_{40} , black line), obtained from I_D response. The X_7 and X_{40} waveform have

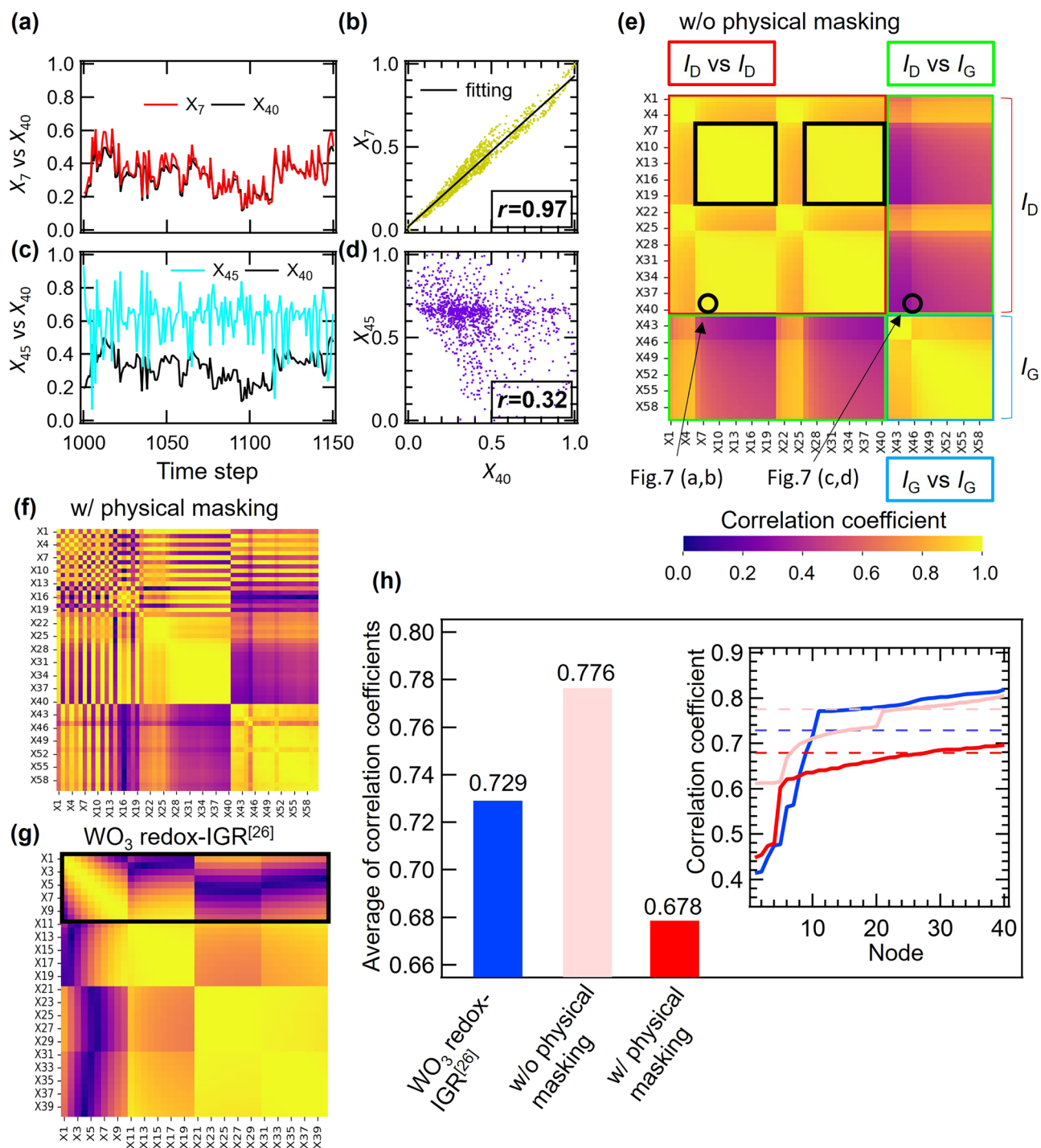


Figure 7. (a) X_7 for I_D (red line) and X_{40} for I_D (black line) wave form. (b) Scatter plot between X_7 and X_{40} with high correlation ($r=0.97$). (c) X_{45} for I_D (blue line) and X_{40} for I_D (black line) wave form. (d) Scatter plot between X_{45} and X_{40} with low correlation ($r=0.32$). (e–g) Correlation coefficient heatmap of w/o and w/ physical masking LiCoO₂ redox-IGR and WO₃ redox-IGR. (h) Distribution and average of correlation coefficients.

almost the same shape, and Fig. 7b shows that they are very strongly correlated, with a correlation coefficient of 0.97. This indicates that the two node states are almost identical, and the reservoirs are not very expressive. On the other hand, the X_{45} and X_{40} waveforms shown in Fig. 7c are very different, with a low correlation coefficient of 0.32 (Fig. 7d). The large difference in the shape of the node states makes the reservoirs more expressive and reduces the error in the tasks²⁶.

Figure 7e–g shows a color map of the correlation coefficients between the nodes of LiCoO₂ redox-IGR and WO₃ redox-IGR²⁶. The results of WO₃ redox-IGR device are shown as a reference for comparison with the performance of LiCoO₂ redox-IGR in the study²⁶. In a LiCoO₂ redox-IGR, nodes 1 to 20 correspond to the data obtained from the I_{D1} , nodes 21 to 40 correspond to the I_{D2} , and nodes 41 to 60 correspond to the I_G . In WO₃

redox-IGR, nodes 1 to 20 correspond to the data obtained from the I_D , and nodes 21 to 40 correspond to the I_G ²⁶. Areas with low correlation coefficients are shown in dark colors, while areas with high correlation coefficients are shown in light colors. Figure 7e shows that the correlation coefficient is particularly low during the pulse intervals ($V_G = 0$ V) when the drain and gate currents are relaxing (regions X_7 to X_{20} and X_{27} to X_{40} in Fig. 7e), which is different from Fig. 7g where the correlation coefficient is low during the application of pulse in WO_3 redox-IGR (X_1 to X_{10} in Fig. 7g). When comparing Fig. 7e,f, it can be seen that physical masking enhances the diversity of reservoir states and decreased the overall correlation coefficient that was suggested in Fig. 2c, mainly the correlation coefficient between nodes obtained from I_{D1} , and that physical masking significantly decreased the NARMA2 score (from $\text{NMSE} = 0.189$ to $\text{NMSE} = 0.054$).

The average values of the correlation coefficients between nodes are listed in order of lower correlation coefficients in right-hand panel of Fig. 7h, while the dotted line is the average value of all nodes. The left-hand part of Fig. 7h shows the average of the correlation coefficients of the LiCoO_2 redox-IGR (with and without physical masking) and the WO_3 redox-IGR, which are 0.776, 0.678 and 0.729, respectively²⁶. The distribution of correlation coefficients and the average values of correlation coefficients in Fig. 7h indicate that the higher dimensionality, achieved by decreasing the correlation between nodes through the application of physical masking, led to significant improvement in IGR performance.

Conclusions

We developed a redox-IGR using a (104) oriented LiCoO_2 thin film so as to overcome the low performance exhibited by previously reported redox-IGR, which is caused by irreversible Li^+ trapping in the WO_3 channel²⁶. The subject LiCoO_2 redox-IGR utilizes the reversible resistance change that results from the redox reaction ($\text{LiCoO}_2 \rightleftharpoons \text{Li}_{1-x}\text{CoO}_2 + x\text{Li}^+ + xe^-$) accompanying the insertion and desorption of Li^+ . In addition to the use of LiCoO_2 , a physical masking technique was developed to improve performance, which it does by time-multiplexing of the input without any extra pre-processing calculation burden. The computational performance of the subject LiCoO_2 redox-IGR was evaluated by performing a second-order nonlinear transformation task and a NARMA2 task. The prediction error was reduced by 72% and the operation speed was increased by 4 times compared to a WO_3 redox-IGR²⁶. The reason for said improvements was investigated in terms of the three aspects that are generally required for RC: short-term memory, nonlinearity, and high dimensionality. Short-term memory was evaluated by determining the MC through a short-term memory task. Although we confirmed that computational performance increased with increasing MC, the MC of the LiCoO_2 redox-IGR was smaller than that of a WO_3 redox-IGR, suggesting that factors other than MC had a significant impact on the high computational performance. Nonlinearity was evaluated by comparing the V_G sweep curves of redox-IGRs. From such sweep curves, we found that the LiCoO_2 redox-IGR showed a strong nonlinear resistance change with respect to V_G . High dimensionality was evaluated by determining the correlation coefficient between the nodes, and it was found that LiCoO_2 redox-IGR had more independent nodes with low correlation coefficients, which led to high computational performance. Neuromorphic computing is of great importance in overcoming the high-power consumption of exhibited by current AI devices. In particular, physical RC has huge potential for realizing excellent compatibility with high computing performance, low power consumption, and small device volume. Our results indicate a promising way to develop high performance neuromorphic circuits consisting not only of nanoionic devices^{55–67}, but also of a wide range of nanomaterials and nanoarchitectonic systems^{59–73}.

Methods

Readout network ridge regression training

When solving time series transformation tasks such as the Second-order nonlinear dynamic equation task and NARMA2 tasks shown in Figs. 3 and 4, the readout network of the IGR is trained by ridge regression. The reservoir state vector $\mathbf{x}(k)$ is acquired from IGR (I_{D1} , I_{D2} , I_G), and the reservoir output $y(k)$ is the linear combination of the readout weight vector \mathbf{w} and $\mathbf{x}(k)$,

$$y(k) = \mathbf{w} \cdot \mathbf{x}(k). \quad (14)$$

Here, $\mathbf{w} = (w_1, w_2, \dots, w_N)$, $\mathbf{x}(k) = (1, X_1(k), X_2(k), \dots, X_N(k))^T$ and N is a reservoir size, respectively. The cost function $J(\mathbf{W})$ in the ridge regression is defined by Eq. (15) as:

$$J(\mathbf{W}) = \frac{1}{2} \sum_{k=1}^T [y_t(k) - y(k)]^2 + \frac{\beta}{2} \sum_{i=0}^N \omega_i^2. \quad (15)$$

Here, T , β and $y_t(k)$ are the data length in the training phase, the ridge parameter and the target output of the task generated by Eqs. (5) and (8), respectively. In this study, reservoir calculations were performed for all tasks with $T = 890$ and $\beta = 2 \times 10^{-3}$. The readout weight $\widehat{\mathbf{W}}$ that minimizes the cost function $J(\mathbf{W})$ is given by following equation:

$$\widehat{\mathbf{W}} = \mathbf{Y}\mathbf{X}^T(\mathbf{X}\mathbf{X}^T + \beta\mathbf{I})^{-1}. \quad (16)$$

Here, $\mathbf{Y} = [y_1(t), y_2(t), \dots, y_t(T)]$, $\mathbf{X}[\mathbf{x}(1), \mathbf{x}(2), \dots, \mathbf{x}(T)]$, and $\mathbf{I}[\subseteq \mathbb{R}^{(N+1) \times (N+1)}]$ are the target output vector, the reservoir state matrix, and the identity matrix, respectively.

Data availability

All data generated or analyzed during this study are included in this published article (and its Supplementary Information files).

Received: 29 June 2023; Accepted: 21 November 2023

Published online: 29 November 2023

References

1. Tanaka, G. *et al.* Recent advances in physical reservoir computing: A review. *Neural Netw.* **115**, 100–123 (2019).
2. Jaeger, H. The ‘echo state’ approach to analysing and training recurrent neural networks—with an Erratum note. *Fraunhofer IAIS* **1**, 1 (2010).
3. Jaeger, H. & Haas, H. Harnessing nonlinearity: Predicting chaotic systems and saving energy in wireless communication. *Science* **304**, 78–80 (2004).
4. Nakane, R., Tanaka, G. & Hirose, A. Reservoir computing with spin waves excited in a garnet film. *IEEE Access.* **6**, 4462–4469 (2018).
5. Nakajima, M. *et al.* Physical deep learning with biologically inspired training method: Gradient-free approach for physical hardware. *Nat. Commun.* **13**, 7847 (2022).
6. Akiyama, T. & Tanaka, G. Computational efficiency of multi-step learning echo state networks for nonlinear time series prediction. *IEEE Access.* **10**, 28535–28544 (2022).
7. Inubushi, M. & Yoshimura, K. Reservoir computing beyond memory–nonlinearity trade-off. *Sci. Rep.* **7**, 10199 (2017).
8. Paquot, Y. *et al.* Optoelectronic reservoir computing. *Sci. Rep.* **2**, 287 (2012).
9. Van der Sande, G., Brunner, D. & Soriano, M. C. Advances in photonic reservoir computing. *Nanophotonics* **6**, 561–576 (2017).
10. Torreon, J. *et al.* Neuromorphic computing with nanoscale spintronic oscillators. *Nature* **547**, 428–431 (2017).
11. Tsunegi, S. *et al.* Physical reservoir computing based on spin torque oscillator with forced synchronization. *Jpn. J. Appl. Phys. Lett.* **114**, 164101 (2019).
12. Jiang, W. *et al.* Physical reservoir computing using magnetic skyrmion memristor and spin torque nano-oscillator. *Jpn. J. Appl. Phys. Lett.* **115**, 192403 (2019).
13. Akashi, N. *et al.* Input-driven bifurcations and information processing capacity in spintronics reservoirs. *Phys. Rev. Res.* **2**, 043303 (2020).
14. Sillin, H. O. *et al.* A theoretical and experimental study of neuromorphic atomic switch networks for reservoir computing. *Nanotechnology* **24**, 384004 (2013).
15. Du, C. *et al.* Reservoir computing using dynamic memristors for temporal information processing. *Nat. Commun.* **8**, 2204 (2017).
16. Moon, J. *et al.* Temporal data classification and forecasting using a memristor-based reservoir computing system. *Nat. Electron.* **2**, 480–487 (2019).
17. Midya, R. *et al.* Reservoir computing using diffusive memristors. *Adv. Intell. Syst.* **1**, 1900084 (2019).
18. Zhu, X., Wang, Q. & Lu, W. D. Memristor networks for real-time neural activity analysis. *Nat. Commun.* **11**, 2439 (2020).
19. Sun, L. *et al.* In-sensor reservoir computing for language learning via two-dimensional memristors. *Sci. Adv.* **7**, 1455 (2021).
20. Hochstetter, J. *et al.* Avalanches and edge-of-chaos learning in neuromorphic nanowire networks. *Nat. Commun.* **12**, 4008 (2021).
21. Zhong, Y. *et al.* Dynamic memristor-based reservoir computing for high-efficiency temporal signal processing. *Nat. Commun.* **12**, 408 (2021).
22. Milano, G. *et al.* In materia reservoir computing with a fully memristive architecture based on self-organizing nanowire networks. *Nat. Mater.* **21**, 195–202 (2022).
23. Nakayama, J., Kanno, K. & Uchida, A. Laser dynamical reservoir computing with consistency: An approach of a chaos mask signal. *Opt. Express* **24**, 8679–8692 (2016).
24. Nakajima, K., Hauser, H., Li, T. & Pfeifer, R. Information processing via physical soft body. *Sci. Rep.* **5**, 10487 (2015).
25. Nishioka, D. *et al.* Edge-of-chaos learning achieved by ion–electron-coupled dynamics in an ion-gating reservoir. *Sci. Adv.* **8**, 1156 (2022).
26. Wada, T. *et al.* A redox-based ion-gating reservoir, utilizing double reservoir states in drain and gate nonlinear responses. *Adv. Intell. Syst.* **5**, 2300123 (2023).
27. Namiki, W. *et al.* *Experimental Demonstration of High-Performance Physical Reservoir Computing with Nonlinear Interfered Spin Wave Multi-Detection* (Wiley, 2022).
28. Yang, J. J., Strukov, D. B. & Stewart, D. R. Memristive devices for computing. *Nat. Nanotechnol.* **8**, 13–24 (2013).
29. Fuller, E. J. *et al.* Parallel programming of an ionic floating-gate memory array for scalable neuromorphic computing. *Science* **364**, 570–574 (2019).
30. Terabe, K., Tsuchiya, T., Yang, R. & Aono, M. Nanoionic devices enabling a multitude of new features. *Nanoscale* **8**, 13873–13879 (2016).
31. Lee, K.-Y. *et al.* Fast magneto-ionic switching of interface anisotropy using Yttria-stabilized zirconia gate oxide. *Nano Lett.* **20**, 3435–3441 (2020).
32. Tsuchiya, T., Nakayama, T. & Ariga, K. Nanoarchitectonics intelligence with atomic switch and neuromorphic network system. *Jpn. J. Appl. Phys. Express* **15**, 100101 (2022).
33. Tsuchiya, T., Terabe, K., Yang, R. & Aono, M. Nanoionic devices: Interface nanoarchitectonics for physical property tuning and enhancement. *Jpn. J. Appl. Phys.* **55**, 1102A4 (2016).
34. Terabe, K., Tsuchiya, T. & Tsuruoka, T. A variety of functional devices realized by ionic nanoarchitectonics, complementing electronics components. *Adv. Electron. Mater.* **8**, 2100645 (2022).
35. Namiki, W., Tsuchiya, T., Takayanagi, M., Higuchi, T. & Terabe, K. Room-temperature manipulation of magnetization angle, achieved with an all-solid-state redox device. *ACS Nano* **14**, 16065–16072 (2020).
36. Tsuchiya, T. *et al.* Neuromorphic transistor achieved by redox reaction of WO₃ thin film. *Jpn. J. Appl. Phys.* **57**, 04FK01 (2018).
37. Wen, R. T., Granqvist, C. G. & Niklasson, G. A. Eliminating degradation and uncovering ion trapping dynamics in electrochromic WO₃ thin films. *Nat. Mater.* **14**, 996 (2015).
38. Wen, R.-T., Arvizu, M. A., Morales-Luna, M., Granqvist, C. G. & Niklasson, G. A. Ion trapping and detrapping in amorphous tungsten oxide thin films observed by real-time electro-optical monitoring. *Chem. Mater.* **28**, 4670–4676 (2016).
39. Takayanagi, M., Tsuchiya, T., Ueda, S., Higuchi, T. & Terabe, K. In situ hard X-ray photoelectron spectroscopy on the origin of irreversibility in electrochromic Li₂WO₃ thin films. *Appl. Surf. Sci.* **568**, 150898 (2021).
40. Fuller, E. J. *et al.* Li-ion synaptic transistor for low power analog computing. *Adv. Mater.* **29**, 1604310 (2017).
41. Wan, X., Tsuruoka, T. & Terabe, K. Neuromorphic system for edge information encoding: Emulating retinal center-surround antagonism by Li-ion-mediated highly interactive devices. *Nano Lett.* **21**, 7938–7945 (2021).
42. Tsuchiya, T. *et al.* The electric double layer effect and its strong suppression at Li⁺ solid electrolyte/hydrogenated diamond interfaces. *Commun. Chem.* **4**, 117 (2021).
43. Matsuda, Y. *et al.* In situ Raman spectroscopy of Li_xCoO₂ cathode in Li/Li₃PO₄/LiCoO₂ all-solid-state thin-film lithium battery. *Solid State Ion.* **335**, 7–14 (2019).
44. Ohnishi, T. & Takada, K. Sputter-deposited amorphous Li₃PO₄ solid electrolyte films. *ACS Omega* **7**, 21199–21206 (2022).
45. Orman, H. J. & Wiseman, P. J. Cobalt(III) lithium oxide, CoLiO₂: Structure refinement by powder neutron diffraction. *Acta Crystallogr. C Struct.* **40**, 12–14 (1984).

46. Tai, Z. *et al.* Few atomic layered lithium cathode materials to achieve ultrahigh rate capability in lithium-ion batteries. *Adv. Mater.* **29**, 1700605 (2017).
47. Ardebili, H., Zhang, J. & Pecht, M. *Encapsulation Technologies for Electronic Applications* (Elsevier, 2018).
48. van Doorn, W. P. T. M. *et al.* Machine learning-based glucose prediction with use of continuous glucose and physical activity monitoring data: The Maastricht Study. *PLoS ONE* **16**, 0253125 (2021).
49. Appeltant, L., Van der Sande, G., Danckaert, J. & Fischer, I. Constructing optimized binary masks for reservoir computing with delay systems. *Sci. Rep.* **4**, 3629 (2014).
50. Akai-Kasaya, M. *et al.* Performance of reservoir computing in a random network of single-walled carbon nanotubes complexed with polyoxometalate. *Neuromorph. Comput. Eng.* **2**, 014003 (2022).
51. Kan, S., Nakajima, K., Asai, T. & Akai-Kasaya, M. Physical implementation of reservoir computing through electrochemical reaction. *Adv. Sci.* **9**, 2104076 (2022).
52. Kan, S. *et al.* Simple reservoir computing capitalizing on the nonlinear response of materials: Theory and physical implementations. *Phys. Rev. Appl.* **15**, 024030 (2021).
53. Milewska, A. *et al.* The nature of the non-metal–metal transition in Li_xCoO_2 oxide. *Solid State Ion.* **263**, 110–118 (2014).
54. Menetrier, M., Saadoun, I., Levasseur, S. & Delmas, C. The insulator–metal transition upon lithium deintercalation from LiCoO_2 : Electronic properties and 7Li NMR study. *J. Mater. Chem. C* **9**, 1135 (1999).
55. Yang, C.-S. *et al.* All-solid-state synaptic transistor with ultralow conductance for neuromorphic computing. *Adv. Funct. Mater.* **28**, 1804170 (2018).
56. Tsuchiya, T., Imura, M., Koide, Y. & Terabe, K. Magnetic control of magneto-electrochemical cell and electric double layer transistor. *Sci. Rep.* **7**, 10534 (2017).
57. Van de Burgt, Y. *et al.* A non-volatile organic electrochemical device as a low-voltage artificial synapse for neuromorphic computing. *Nat. Mater.* **16**, 414–418 (2017).
58. Tsuchiya, T., Moriyama, S., Terabe, K. & Aono, M. Modulation of superconducting critical temperature in niobium film by using all-solid-state electric-double-layer transistor. *Jpn. J. Appl. Phys.* **107**, 013104 (2015).
59. Li, Y. *et al.* Filament-free bulk resistive memory enables deterministic analogue switching. *Adv. Mater.* **32**, 2003984 (2020).
60. Isoda, Y. *et al.* Electrochemical control and protonation of the strontium iron oxide SrFeO_3 , by using proton-conducting electrolyte. *Jpn. J. Appl. Phys.* **120**, 091601 (2022).
61. Wada, T. *et al.* In situ manipulation of perpendicular magnetic anisotropy in half-metallic NiCo_2O_4 thin film by proton insertion. *Jpn. J. Appl. Phys.* **61**, 1002 (2022).
62. Tsuchiya, T. *et al.* Direct observation of redox state modulation at carbon/amorphous tantalum oxide thin film hetero-interface probed by means of in situ hard X-ray photoemission spectroscopy. *Solid State Ion.* **253**, 110–118 (2013).
63. Tan, A. J. *et al.* Hydration of gadolinium oxide (GdO_x) and its effect on voltage-induced co oxidation in a Pt/Co/GdO_x/Au heterostructure. *Phys. Rev. Mater.* **3**, 064408 (2019).
64. Lu, Q. *et al.* Electrochemically triggered metal–insulator transition between VO_2 and V_2O_5 . *Adv. Funct. Mater.* **28**, 1803024 (2018).
65. Bauer, U. *et al.* Magneto-ionic control of interfacial magnetism. *Nat. Mater.* **14**, 174–181 (2015).
66. Lübber, M. *et al.* Design of defect-chemical properties and device performance in memristive systems. *Sci. Adv.* **6**, 9079 (2020).
67. Takayanagi, M. *et al.* Accelerated/decelerated dynamics of the electric double layer at hydrogen-terminated diamond/ Li^+ solid electrolyte interface. *Mater. Today Phys.* **31**, 101006 (2023).
68. Li, Y. *et al.* Low-voltage, CMOS-free synaptic memory based on Li_xTiO_2 redox transistors. *ACS Appl. Mater. Interfaces* **11**, 38982–38992 (2019).
69. Song, J., Kawakami, K. & Ariga, K. Nanoarchitectonics in combat against bacterial infection using molecular, interfacial, and material tools. *Curr. Opin. Coll. Int. Sci.* **65**, 101702 (2023).
70. Ariga, K. Materials nanoarchitectonics: Collaboration between Chem, Nano and Mat. *ChemNanoMat* **1**, 202300120 (2023).
71. Matsumoto, M., Sutrisno, L. & Ariga, K. Covalent nanoarchitectonics: Polymer synthesis with designer structures and sequences. *J. Polym. Sci.* **61**, 861–869 (2023).
72. Ariga, K. Molecular machines and microrobots: Nanoarchitectonics developments and on-water performances. *Micromachines* **14**, 25 (2022).
73. Shrestha, L. K. *et al.* Biomass nanoarchitectonics for supercapacitor applications. *J. Oleo Sci.* **72**, 11–32 (2023).

Acknowledgements

This work was in part supported by Japan Society for the Promotion of Science (JSPS) KAKENHI Grant Number JP22H04625 (Grant-in-Aid for Scientific Research on Innovative Areas “Interface Ionics”), and JP22KJ2799 (Grant-in-Aid for JSPS Fellows). A part of this work was supported by the Iketani Science and Technology Foundation, the Yazaki Memorial Foundation for Science and Technology and Kurata Grants from The Hitachi Global Foundation.

Author contributions

K.S., D.N., W.N., T.T., and K.T. conceived the idea for the study. K.S. and D.N. designed the experiments. K.S., D.N. and T.T. wrote the paper. K.S. carried out the experiments. K.S. prepared the samples. K.S., D.N., W.N., and T.T. analyzed the data. All authors discussed the results and commented on the manuscript. K.T. directed the projects.

Competing interests

The authors declare no competing interests.

Additional information

Supplementary Information The online version contains supplementary material available at <https://doi.org/10.1038/s41598-023-48135-z>.

Correspondence and requests for materials should be addressed to T.T.

Reprints and permissions information is available at www.nature.com/reprints.

Publisher’s note Springer Nature remains neutral with regard to jurisdictional claims in published maps and institutional affiliations.



Open Access This article is licensed under a Creative Commons Attribution 4.0 International License, which permits use, sharing, adaptation, distribution and reproduction in any medium or format, as long as you give appropriate credit to the original author(s) and the source, provide a link to the Creative Commons licence, and indicate if changes were made. The images or other third party material in this article are included in the article's Creative Commons licence, unless indicated otherwise in a credit line to the material. If material is not included in the article's Creative Commons licence and your intended use is not permitted by statutory regulation or exceeds the permitted use, you will need to obtain permission directly from the copyright holder. To view a copy of this licence, visit <http://creativecommons.org/licenses/by/4.0/>.

© The Author(s) 2023